Optimal design for non-Newtonian flows using a topology optimization approach

Georg Pingen [a,*], Kurt Maute [b]

[a] *Department of Mechanical and Aerospace Engineering, University of Colorado, Colorado Springs, CO 80933, USA*
[b] *Department of Aerospace Engineering Sciences, University of Colorado, Boulder, CO 80309, USA*

ARTICLE INFO

ABSTRACT

We study non-Newtonian effects on the layout and geometry of flow channels using a material distribution based topology optimization approach. The flow is modeled with the single-relaxation hydrodynamic lattice Boltzmann method, and the shear dependence of viscosity is included through the Carreau–Yasuda model for non-Newtonian fluids. To represent the viscosity of blood in this model, we use non-Newtonian similarity. Further, we introduce a scaling to decrease the effects of the non-Newtonian model in porous regions in order to stabilize the coupling of the LBM porosity and non-Newtonian flow models. For the resulting flow model, we derive the non-Newtonian sensitivity analysis for steady-state conditions and illustrate the non-Newtonian effect on channel layouts for a 2D dual-pipe design problem at different Reynolds numbers.

© 2009 Elsevier Ltd. All rights reserved.

1. Introduction

The effects of non-Newtonian fluid properties on biomedical design problems are of considerable interest and have been studied, for example, by Abraham et al. [1], Gijsen et al. [2], Lauprecht and Perktold [3], Lukáčová-Medviďová and Zaušková [4], and Boyd and Buick [5]. In a few instances, shape optimization techniques have been utilized to study the difference in optimal designs assuming Newtonian and non-Newtonian flow models. Shape optimization of an arterial bypass has been studied by Abraham et al. [1] and Quarteroni and Rozza [6], leading to differences in optimum bypass graft angles and entrance regions for Newtonian and non-Newtonian fluids. Further, optimal shape design of rotary blood pump components has been studied by Antaki et al. [7]. While these references have considered the optimal shape modification of existing designs under non-Newtonian flow considerations, the present work investigates the effect of a non-Newtonian model on the overall layout and geometry of flow channels. Namely, a topology optimization approach is utilized to identify fundamental differences in design topologies between Newtonian and non-Newtonian flows, and to optimize the overall layout of fluidic devices undergoing non-Newtonian flow phenomena. The conceptual differences between the layout of flow channels optimized for Newtonian and non-Newtonian flow regimes are illustrated through an example of a dual-pipe inlet/outlet flow.

Topology optimization for fluids was introduced by Borrvall and Petersson [8]. In recent years it has received increased attention due to its general applicability to a wide range of problems in hydrodynamics and beyond, using the Stokes and Navier–Stokes equations [9–14]. The authors and co-workers have developed a topology optimization framework for low Reynolds number flows based on the lattice Boltzmann method [15–17]. The LBM features algorithmic simplicity, parallel scalability, inherent use of immersed boundary methods, a well suited porosity model for topology optimization, and

---

* Corresponding author.
  E-mail address: gpingen@eas.uccs.edu (G. Pingen).

applicability beyond traditional hydrodynamics. To account for non-Newtonian flow phenomena, this topology optimization framework is augmented by the Carreau–Yasuda (C–Y) model for the lattice Boltzmann method [18] in the present study. To ensure the stability of the coupled porosity and non-Newtonian LBM models in areas of high porosity, a scaling of the non-Newtonian model is introduced to reduce the non-Newtonian effects in porous regions. Further, the LBM sensitivity analysis is modified for non-Newtonian flows and non-Newtonian similarity is used to model blood flows with the standard (single relaxation) LBM on small meshes. It is the goal of this work to extend the authors' LBM topology optimization algorithm to non-Newtonian flows, performing a proof of concept study that illustrates the basic influence of non-Newtonian flow behavior on designs.

The lattice Boltzmann method for non-Newtonian flows is discussed in Section 2, including a discussion on non-Newtonian similarity (Section 2.2) and the coupling of the porosity and non-Newtonian LBM models (Section 2.3). The resulting non-Newtonian optimization problem and corresponding sensitivity analysis are discussed in Section 3. The differences between Newtonian and non-Newtonian optimal designs are illustrated for a dual-pipe at various Reynolds numbers in Section 4.

2. The lattice Boltzmann method for topology optimization

The lattice Boltzmann method (LBM) has become a popular alternative to conventional, Navier–Stokes based computational methods for a variety of problems in fluid dynamics (cf., e.g., [19–21]). The hydrodynamic lattice Boltzmann method approximates the Navier–Stokes equations and is based on the discretized Boltzmann equation, constituting a two step computational process:

$$\text{Collision} - \mathbf{\Omega}: \quad \widetilde{f_\alpha}(\mathbf{x}_i, t) = f_\alpha(\mathbf{x}_i, t) - \frac{1}{\tau}[f_\alpha(\mathbf{x}_i, t) - f_\alpha^{eq}(\mathbf{x}_i, t)]. \tag{1}$$

$$\text{Propagation} - \mathbf{\Pi}: \quad f_\alpha(\mathbf{x}_i + \delta t \mathbf{e}_\alpha, t + \delta t) = \widetilde{f_\alpha}(\mathbf{x}_i, t). \tag{2}$$

In (1) and (2), $\mathbf{e}_\alpha$ is the velocity vector, f_α is the distribution function associated with the corresponding velocity $\mathbf{e}_\alpha$ using the D2Q9 lattice model in the current study, $\mathbf{x}_i$ represents the location in physical space, $\mathbf{e}_\alpha \delta t$ is the lattice spacing, and δt is the time step. Further,

$$\tau(\dot{\gamma}) = \frac{\lambda}{\delta t} = \frac{\nu(\dot{\gamma})}{c_s^2 \delta t} + \frac{1}{2}, \tag{3}$$

is the dimensionless relaxation time, which for non-Newtonian problems depends on the shear-rate $\dot{\gamma}$. The relationship between viscosity ν and relaxation time τ is obtained from a Chapman–Enskog expansion of the Lattice Boltzmann equations [22] as

$$\nu(\dot{\gamma}) = (\tau(\dot{\gamma}) - 1/2)c_s^2 \delta t. \tag{4}$$

For low Mach number flow conditions, the equilibrium distribution function f^{eq} in Eq. (1) can be derived by a Taylor series expansion of the Maxwell–Boltzmann equilibrium distribution:

$$f_\alpha^{eq} = w_\alpha \rho \left[1 + 3(\mathbf{e}_\alpha \cdot \mathbf{u}) + \frac{9}{2}(\mathbf{e}_\alpha \cdot \mathbf{u})^2 - \frac{3}{2}\mathbf{u}^2 \right], \tag{5}$$

where ρ represents the macroscopic density, the vector $\mathbf{u}$ is the macroscopic velocity, and w_α are lattice weights that depend on the lattice geometry. The macroscopic parameters, such as density, velocity, pressure, and viscosity, are evaluated by the statistical moments of the distribution function f.

For gradient-based topology optimization of fluids, a continuous transition from fluid to solid and vice versa is required and generally achieved through a Brinkman penalization [23]. This was done first by Borrvall and Petersson [8], modifying the Stokes equation with a Brinkman term to model the flow through porous media [24]. Similarly, the authors [15] adopted and augmented the porosity model originally introduced by Spaid and Phelan [25] for LBM topology optimization purposes. Here, the macroscopic velocity is rescaled during the collision step (1) for all lattice nodes occupied by the porous medium,

$$\tilde{\mathbf{u}}(t, \mathbf{x}) = (1 - \mathbf{p}(\mathbf{x})^\kappa)\mathbf{u}(t, \mathbf{x}), \tag{6}$$

where $\mathbf{p}(\mathbf{x})$ is related to the inverse permeability in the domain and $\tilde{\mathbf{u}}(t, \mathbf{x})$ is substituted into the equilibrium distribution function (5) instead of $\mathbf{u}$. This porosity model permits a smooth transition from fluid sites ($\mathbf{p}(\mathbf{x}) = 0$) into solid sites ($\mathbf{p}(\mathbf{x}) = 1$) as needed for gradient-based topology optimization. The shaping factor κ has been introduced by the authors [17] in order to improve the convergence properties of the design optimization process. Numerical studies have shown best results for $\kappa \simeq 3$. This modification from the original porosity model by Spaid and Phelan is justified as we are not primarily concerned with the accurate modeling of porous flows, but use porosity in order to transition from fluid to solid and vice-versa.

For topology optimization under steady-state flow conditions, the governing flow equations are expressed by the following fixed-point problem:

$$\mathbf{R}(\mathbf{f}, \mathbf{p}) = \mathbf{M}(\mathbf{f}, \mathbf{p}) - \mathbf{f} = \mathbf{0}, \tag{7}$$

where $\mathbf{R}$ denotes the residual vector. The operator $\mathbf{M}$ performs one collision $\mathbf{\Omega}$ (1) and one propagation $\mathbf{\Pi}$ (2) step, which is exactly what is needed to advance the flow to the next time step. The fixed-point problem (7) is solved by advancing the transient lattice Boltzmann equations (1) and (2) in time until the flow is converged to steady-state, that is, the difference between two or more successive flow states is negligible. The convergence criterion used in this work can be written as follows,

$$\frac{\mathbf{R}}{\mathbf{R}_{ref}} = \frac{\|\mathbf{f}_t - \mathbf{f}_{t-1}\|_\infty}{\|\mathbf{f}_1 - \mathbf{f}_0\|_\infty} \le \varepsilon \tag{8}$$

where $\mathbf{R}_{ref}$ is the reference residual for the initial time step, and for $\varepsilon > 0$. For the presented examples, we choose $\varepsilon = 10^{-10}$, resulting in approximately 10,000 to 100,000 iterations, depending on flow parameters, until flow convergence is achieved. A strict convergence is used to ensure sufficient convergence of the macroscopic variables and forces, in particular the pressure-drop used as an objective in the presented work.

2.1. Non-Newtonian flow

In recent years, the lattice Boltzmann method has been applied to non-Newtonian flows, in particular the modeling of blood flow via power-law models, the Casson model, and the Carreau–Yasuda model for shear thinning fluids [18,26–28]. All models are based on introducing a shear-rate $\dot{\gamma}$ dependent viscosity $\nu(\dot{\gamma})$ in the standard lattice BGK equation (1) through the relaxation time $\tau(\dot{\gamma})$ (3) in the lattice Boltzmann algorithm. The current study uses the Carreau–Yasuda (C–Y) model.

Following the discussion by Boyd et al. [18], the shear rate is defined as

$$\dot{\gamma} = 2\sqrt{D_{II}}, \tag{9}$$

where D_{II} is the second invariant of the strain tensor $S_{\alpha\beta}$:

$$D_{II} = \sum_{i,j=1}^{l} S_{ij} S_{ij}. \tag{10}$$

Here, l is the dimension of the problem. Considering 2D flows, the shear rate can be expressed in terms of the strain tensor as:

$$\dot{\gamma} = 2\sqrt{S11^2 + S22^2 + 2S12^2}. \tag{11}$$

It is shown by Artoli [29], that the strain rate tensor, macroscopically defined as

$$S_{ij} = \frac{1}{2}(\nabla_j u_i + \nabla_i u_j), \tag{12}$$

can be computed locally as

$$S_{ij} = -\frac{3}{2\tau} \sum_\alpha f_\alpha^{(1)} \vec{e}_{\alpha i} \vec{e}_{\alpha j}, \tag{13}$$

where $f_\alpha^{(1)}$ is approximated as the non-equilibrium distribution function $f_\alpha^{(1)} \approx f_\alpha^{neq} = f_\alpha - f_\alpha^{eq}$.

Thus, the shear rate $\dot{\gamma}$ can be computed locally as a function of the distribution function values f_α. This shear-rate is then used in the C–Y model to obtain the shear-rate dependent viscosity as

$$\nu(\dot{\gamma}) = \nu_\infty + (\nu_0 - \nu_\infty)[1 + (\lambda\dot{\gamma})^a]^{(n-1)/a}, \tag{14}$$

where a, n, and λ are constant parameters with λ being the characteristic non-Newtonian relaxation time. In this study we only consider blood flow and use the model parameters given by Abraham et al. [1]:

- $a = 0.64$
- $n = 0.2128$
- $\lambda = 8.2$ s
- $\mu_\infty = 0.0035$ Pa s, leading to $\nu_\infty = 0.0000033$ m^2/s for $\rho_{blood} = 1060$ kg/m^3
- $\mu_0 = 0.1600$ Pa s, leading to $\nu_0 = 0.000151$ m^2/s.

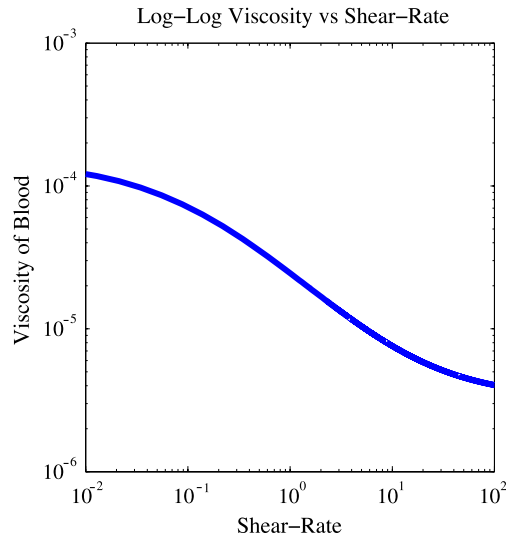Utilizing these parameters leads to the viscosity/shear-rate relation illustrated in Fig. 1.

Fig. 1. Log–log plot of shear-rate dependent viscosity for blood using the Carreau–Yasuda model.

2.2. Non-Newtonian similarity

The Carreau–Yasuda parameters are introduced into the LBM flow model in lattice units. The conversion can be performed with the following relations:

$$
\begin{aligned}
\Delta x &= \frac{L}{N}, \\
\Delta t &= \frac{\Delta x c_s}{a_{sb}}, \\
v^{real} &= \frac{(\Delta x)^2}{\Delta t} v^{lb}, \\
\vec{u}^{real} &= \frac{\Delta x}{\Delta t} \vec{u}^{lb}, \\
\lambda^{real} &= \Delta t \lambda^{lb}.
\end{aligned}
\tag{15}
$$

Here, L is the characteristic length, N is the number of lattice units along the characteristic length, and $a_{sb} = 1500$ m/s is the speed of sound in blood. Using an average value for the diameter of a human artery of $L \approx 4.0$ mm and an LBM channel width of $N = 10$ LBM units, one finds $v_\infty^{lb} \approx 3.198 \cdot 10^{-6}$, which results in a required LBM relaxation time of:

$$
\tau \approx 0.500001.
\tag{16}
$$

However, the practical stability limit of the single relaxation time LBM (SRT-LBM) is $\tau \approx 0.502$ [30], leading to a minimum achievable LBM viscosity of $v_{min}^{lb} \approx 0.0066$.

For Newtonian flows, the inability of the SRT-LBM to model low viscosity flows is overcome by utilizing the Reynolds number similarity, permitting the scaling of both velocity and viscosity while maintaining a constant Reynolds number and thus similar flow behavior. The Reynolds number similarity must be augmented for non-Newtonian fluids, since the shear-rate and thus the non-Newtonian flow properties depend on the velocity gradients through equations (11) and (12). These non-Newtonian flow properties can be scaled by maintaining a constant Deborah number [31], De, defined as the ratio between the characteristic non-Newtonian relaxation time λ and characteristic time for the problem $L/\vec{u}$:

$$
De = \frac{\lambda \vec{u}}{L}.
\tag{17}
$$

Using the scaling:

$$
\begin{aligned}
\vec{u}_s &= F_s \vec{u}, \\
v_s &= F_s v, \\
L_s &= L,
\end{aligned}
\tag{18}
$$

where F_s is the scaling factor, leads to
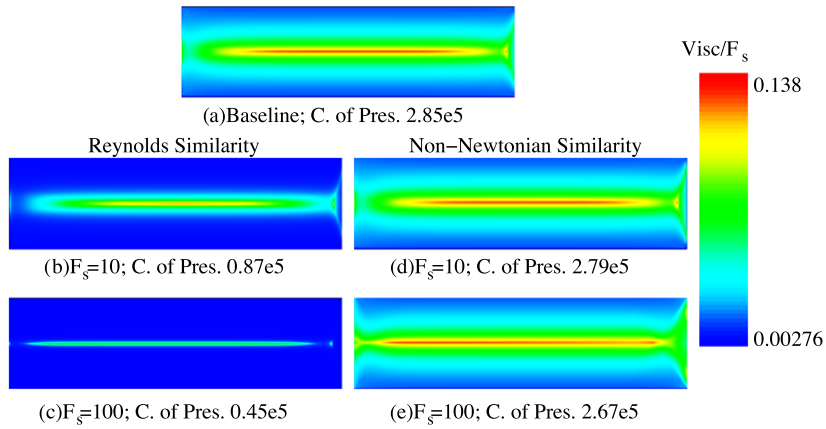
$$
\lambda_s = \frac{\lambda}{F_s}.
\tag{19}
$$

Fig. 2. Non-Newtonian similarity illustrated with viscosity contours for a 500 × 100 flow channel at $Re = 1$. (a) Baseline blood flow, (b) and (c) Reynolds similarity, and (d) and (e) non-Newtonian similarity. Small differences between non-Newtonian similarity results originate from the flow boundaries.
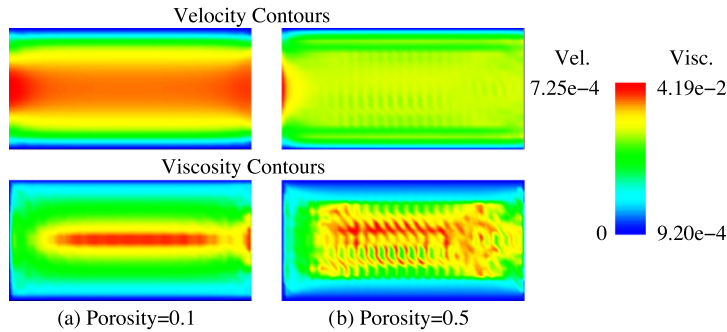

Fig. 3. Illustration of the unsteady behavior caused by the coupling of the LBM porosity and non-Newtonian flow models at intermediate to large porosities. (a) Velocity and viscosity contours for a uniform porosity of $p = 0.1$. (b) Velocity and viscosity contours for a uniform porosity of $p = 0.5$.

The effect of non-Newtonian scaling (constant Re and De) is visualized in Fig. 2. Fig. 2a shows the viscosity contours and coefficient of pressure for C–Y blood flow through a 500 × 100 flow channel at $Re = 1$, considered our baseline result. Application of a Newtonian Reynolds similarity leads to incorrect non-Newtonian behavior as seen from the viscosity contours in Fig. 2b and c for a velocity and viscosity scaling by factors of $F_s = 10$ and $F_s = 100$, respectively. Fig. 2d and e show the corresponding viscosity contour plots for non-Newtonian scaling by the same factors, showing that the correct non-Newtonian viscosities from the baseline example are recovered except for small differences due to boundary effects.

2.3. Effects of coupling porosity and non-Newtonian LBM models

In developing the presented non-Newtonian topology optimization framework, we have observed that the coupling of porosity and shear-rate dependent flow leads to unsteady flow behavior for intermediate to large porosity values, **p**. This is illustrated in Fig. 3 which compares the viscosity distribution for blood flow at $Re = 10$ in a 50 × 20 channel for a uniform porosity distribution of **p** = 0.1 in Fig. 3a and **p** = 0.5 in Fig. 3b, showing unsteady/non-converged behavior for **p** = 0.5.

This behavior is a side effect of the porosity model, which modifies only the equilibrium distribution function f_α^{eq}. On the other hand, the shear-rate needed for the non-Newtonian model depends on the non-equilibrium distribution function $f_\alpha^{neq} = f_\alpha - f_\alpha^{eq}$, which is used to locally determine velocity gradients in LBM. Therefore, scaling the velocity in f_α^{eq} through the porosity model leads to an "inconsistent" modification of the velocity gradients, which results in an oscillatory flow behavior.

For topology optimization of fluids, we are interested primarily in final designs that consist of pure fluid and pure solid states. The porosity model is utilized to continuously transition between the two states. We can overcome the unsteady behavior caused by the coupling of porosity and non-Newtonian LBM models by reducing the non-Newtonian effects in areas of high porosity. For simplicity, we introduce a scaling $((1 - \mathbf{p})^\kappa)$ analogous to that in the porosity model (6) to continuously activate the non-Newtonian model, leading to the following modification of the viscosity/shear-rate relation (14):

$$\nu(\dot{\gamma}) = \nu_\infty + (\nu_0 - \nu_\infty)(1 - \mathbf{p})^\kappa [1 + (\lambda\dot{\gamma})^a]^{(n-1)/a}. \tag{20}$$
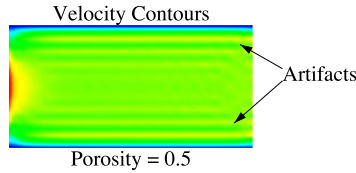
Fig. 4. Steady-State velocity contours at a uniform porosity of $p = 0.5$ obtained with porosity dependent scaling of the non-Newtonian flow properties.
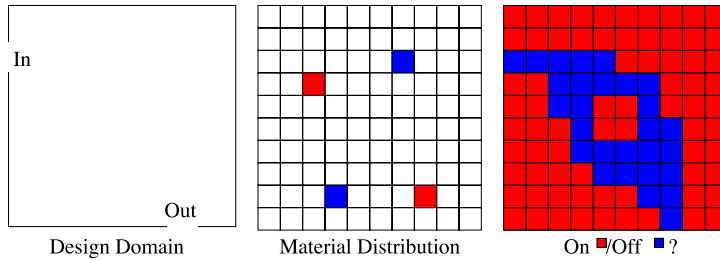

Fig. 5. Conceptual illustration of material distribution based topology optimization for a pipe-bend.

Thus, when $p = 1$ the material is fully solid and Newtonian in nature. When $p = 0$ the material is fully fluid and non-Newtonian in nature. This scaling is justified by the observation that porous material primarily occurs along the flow boundaries where velocity gradients are high and non-Newtonian effects are minimal, and in regions where velocities are approximately zero. Implementing this porosity-based scaling of the non-Newtonian model (20) leads to converged flow behavior as shown in Fig. 4 for the 50×20 flow channel at $Re = 10$ with a uniform porosity distribution of $\mathbf{p} = 0.5$. However, the resulting velocity distribution includes artifacts, e.g., "bands" of higher velocities. While interesting and deserving further study, these artifacts are not essential for the present study, as we utilize porous flows to transition from fluid to solid, and are not primarily interested in correctly modeling flows with intermediate porosities.

3. Topology optimization of non-Newtonian fluids

The optimization problems considered in this study can be formulated as follows:

$$\min_{\mathbf{s}} \mathcal{F}(\mathbf{s}, \mathbf{f}(\mathbf{s})),$$
$$\text{s.t. } \gamma_F(\mathbf{s}) \leq \gamma_{max}, \tag{21}$$

where, $\mathcal{F}$ is a particular performance (objective) functional, $\mathbf{s}$ is the vector of design variables mapped into the local LBM porosities $\mathbf{s} \rightarrow \mathbf{p}$, and $\gamma_F \leq \gamma_{max}$ is a constraint on the design. The distribution function $\mathbf{f}(\mathbf{s})$ is treated as a dependent variable of the design variables $\mathbf{s}$ and determined by solving the state equations (7) that explicitly depend on the LBM porosities $\mathbf{p}$. The porosity distribution in a given design domain is discretized by elements with a locally constant porosity (see Fig. 5). Each element can continuously vary from fluid to solid and vice versa. The resulting optimization problem (21) is continuous and smooth in the optimization variables $\mathbf{s}$ and can be solved with any large-scale gradient-based optimization algorithm. In this study, we use the Globally Convergent Method of Moving Asymptotes (GCMMA) by Svanberg [32], a sequential convex approximation-based algorithm. Here, globally convergent refers to converging to a Karush–Kuhn–Tucker (KKT) point from any initial design that satisfies the bound constraint. GCMMA is not guaranteed to converge to the global optimum.

While objectives such as a shear-stress relation to blood clotting/coagulation will be considered in future applications of the presented topology optimization approach, the present study uses a pressure drop objective to allow for comparison to results published for Newtonian flows [8,15]. The loss of total pressure or pressure drop $\mathcal{PD}$ between fluid inlets and fluid outlets is defined as:

$$\mathbf{F} = \mathcal{PD} = \int_{in} \left[p + \frac{\rho}{2} |\mathbf{v}|^2 \right] - \int_{out} \left[p + \frac{\rho}{2} |\mathbf{v}|^2 \right]. \tag{22}$$

Further, we use a volume constraint, limiting the amount of fluid and thus driving the porosity distribution towards the upper and lower bounds, i.e., a fluid–solid solution with little intermediate values. We prescribe that, at most, a given fraction of the design domain volume, γ_F, is allowed to be occupied by fluid, and the remainder must be solid:

$$\gamma_F \leq \sum_i (1 - p_i^\kappa), \tag{23}$$

where κ is the polynomial shaping introduced for the porosity condition (6). In addition, we enforce a symmetric outlet flow-rate for the dual-pipe example in Section 4.

A direct mapping between design variables and LBM porosities $\mathbf{p} = \mathbf{s}$ may lead to highly oscillatory porosity distributions. To mitigate this effect, the authors [17] have introduced a mapping that leads to a smoother porosity distribution. Each design variable is located in the center between four lattice nodes, leading to:

$$p_{x,y} = \frac{s_{x-1/2,y-1/2} + s_{x-1/2,y+1/2} + s_{x+1/2,y-1/2} + s_{x+1/2,y+1/2}}{4}. \tag{24}$$

3.1. Sensitivity analysis

The derivatives of the performance functional $\mathcal{F}$ in the optimization problem (21) are computed by the adjoint method, owing to the large number of design variables. The derivative of the objective function $\mathcal{F}$ with respect to the design variables $\mathbf{s}$ is written as follows:

$$\frac{\mathrm{d}\mathcal{F}}{\mathrm{d}s_j} = \frac{\partial \mathcal{F}}{\partial s_j} - \left[\left(\frac{\partial \mathbf{R}}{\partial \mathbf{f}} \right)^{-t} \frac{\partial \mathcal{F}}{\partial \mathbf{f}} \right]^t \frac{\partial \mathbf{R}}{\partial p_i} \frac{\partial p_i}{\partial s_j} \tag{25}$$

where $\mathbf{f}$ is the state vector at steady-state and $(\partial \mathbf{R}/\partial \mathbf{f})$ is the Jacobian of the LBM fixed-point system (7). Solving the adjoint sensitivity equation (25) requires the evaluation of four partial derivatives: $\partial \mathcal{F}/\partial s_j$, $\partial \mathcal{F}/\partial \mathbf{f}$, $\partial \mathbf{R}/\partial p_i$, and $\partial \mathbf{R}/\partial \mathbf{f}$. Pingen et al. [17] have presented an adjoint method evaluating these derivatives based on the Newtonian lattice Boltzmann method. Here we focus on the LBM Jacobian $(\partial \mathbf{R}/\partial \mathbf{f})$ and its extension to non-Newtonian flows. For the current pressure drop objective $\partial \mathcal{F}/\partial s_j = 0$ and $\partial \mathcal{F}/\partial \mathbf{f}$ is equivalent to the Newtonian case. The derivative $\partial \mathbf{R}/\partial p_i$ is similar to the Jacobian and the terms can be determined by following an analogous procedure.

The transposed Jacobian of the LBM fixed-point system (7), $(\partial \mathbf{R}/\partial \mathbf{f})^{\mathrm{T}}$, is expanded as,

$$\left(\frac{\partial \mathbf{R}}{\partial \mathbf{f}} \right)^{\mathrm{T}} = \left(\frac{\partial \mathbf{M}}{\partial \mathbf{f}} \right)^{\mathrm{T}} - \mathbf{I}. \tag{26}$$

Here, $(\partial \mathbf{M}/\partial \mathbf{f})^{\mathrm{T}}$ is a function of the operator $\mathbf{M}$, which performs one collision $\mathbf{\Omega}$ and one propagation operation $\mathbf{\Pi}$. Similarly $(\partial \mathbf{M}/\partial \mathbf{f})^{\mathrm{T}}$ is separated into its collision and propagation components:

$$\left(\frac{\partial \mathbf{M}}{\partial \mathbf{f}} \right)^{\mathrm{T}} = \left(\frac{\partial \mathbf{\Pi}}{\partial \mathbf{f}} \right)^{\mathrm{T}} \circ \left(\frac{\partial \mathbf{\Omega}}{\partial \mathbf{f}} \right)^{\mathrm{T}}. \tag{27}$$

For the sensitivity analysis of non-Newtonian flows, only the sensitivity analysis of the collision step must be augmented, as no changes are made to the propagation step. The propagation Jacobian effectively shifts rows in the collision operator, just as the propagation step moves distribution functions to neighboring nodes.

The collision component is computed locally at each node and expressed as:

$$\frac{\partial \mathbf{\Omega}}{\partial \mathbf{f}} = \frac{\partial \widetilde{f_\alpha}}{\partial f_\beta} = \underbrace{\frac{\partial f_\alpha}{\partial f_\beta}}_{\text{I}} - \frac{1}{\tau} \underbrace{\left[\frac{\partial f_\alpha}{\partial f_\beta} - \frac{\partial f_\alpha^{eq}}{\partial f_\beta} \right]}_{\text{II}} - \underbrace{\frac{\partial \frac{1}{\tau}}{\partial f_\beta}}_{\text{III}} [f_\alpha - f_\alpha^{eq}], \tag{28}$$

where α and β represent the directions of the discretized velocity space and the partial derivative $\partial f_\alpha/\partial f_\beta = 1$ if $\alpha = \beta$ and zero otherwise. For this non-Newtonian Jacobian of the collision step (28), only term III has been added due to the shear-rate dependent relaxation time. Solving the viscosity relation (4) for $(1/\tau)$

$$\frac{1}{\tau(\dot{\gamma})} = \frac{2}{2\nu(\dot{\gamma})c_s^{-2} + 1}, \tag{29}$$

the derivative term $(\partial \frac{1}{\tau}/\partial f_\beta)$ can be evaluated as:

$$\frac{\partial \frac{1}{\tau(\dot{\gamma})}}{\partial f_\beta} = \frac{-2}{[2\nu(\dot{\gamma})c_s^{-2} + 1]^2} 6 \frac{\partial \nu(\dot{\gamma})}{\partial f_\beta}. \tag{30}$$

Here, $(\partial \nu(\dot{\gamma})/\partial f_\beta)$ is given by,

$$\frac{\partial \nu(\dot{\gamma})}{\partial f_\beta} = \frac{n-1}{a} (\nu_0 - \nu_{\inf})(1-p)^\kappa [1 + (\lambda \dot{\gamma})^a]^{[(n-1)/a]-1} a(\lambda \dot{\gamma})^{a-1} \lambda \frac{\partial \dot{\gamma}}{\partial f_\beta}, \tag{31}$$
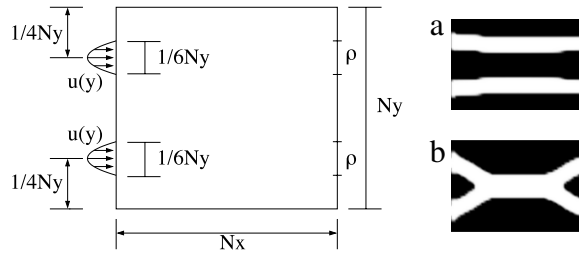
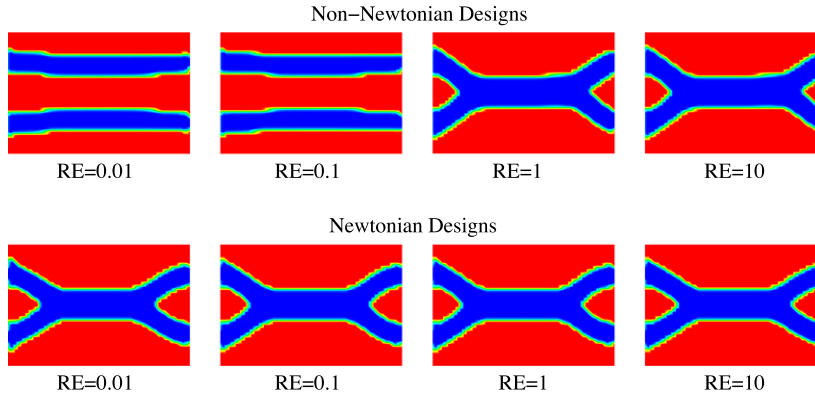**Fig. 6.** Dual pipe design domain with inlet, outlet, and symmetry conditions.

Fig. 7. Comparison between non-Newtonian and Newtonian optimal designs at $Re = 0.01, 0.1, 1.0,$ and 10.

with

$$\frac{\partial \dot{\gamma}}{\partial f_\beta} = \frac{1}{\sqrt{S_{11}^2 + S_{22}^2 + 2S_{12}^2}} \left(2S_{11} \frac{\partial S_{11}}{\partial f_\beta} + 2S_{22} \frac{\partial S_{22}}{\partial f_\beta} + 4S_{12} \frac{\partial S_{12}}{\partial f_\beta} \right), \tag{32}$$

$$\frac{\partial S_{ij}}{\partial f_\beta} = -\frac{3}{2\tau} \sum_\alpha \vec{e}_{\alpha i} \vec{e}_{\alpha j} \frac{\partial f_\alpha^{(1)}}{\partial f_\beta}, \tag{33}$$

and $(\partial f_\alpha^{(1)}/\partial f_\beta)$ given by term II in the collision Jacobian (28), which is explicitly derived in the authors recent work [17].

4. Example: Dual-pipe

A dual-pipe flow topology optimization problem, as illustrated in Fig. 6, was first used by Borrvall and Petersson [8] for topology optimization of fluids, showing different design topologies (dual pipes vs merged pipes) for short and long design domains, respectively. The problem has also been used by the authors and co-workers [15] to validate the Newtonian LBM topology optimization framework. The design has two inlets and two outlet ports with symmetric inlet and outlet flow, and the fluid volume γ_F is restricted to 33% of the design domain. For the non-Newtonian flow, we use the C–Y properties of blood given by Abraham et al. [1]. Further, all design optimizations are initialized with a uniform porosity distribution of $\mathbf{p} = 0.1$.

The example illustrates the ability of topology optimization to identify designs with conceptually different channel layouts and geometry under Newtonian and non-Newtonian flow modes. We show results for Newtonian and non-Newtonian designs at different Reynolds numbers and perform a cross-comparison between the results. Finally, we briefly compare non-Newtonian optimal designs at $Re = 0.01$ for three different mesh resolutions: 30×20, 60×40, and 120×80. Topology optimization results for both non-Newtonian and Newtonian flows on a 60×40 mesh are shown in Fig. 7 for Reynolds numbers of $Re = 0.01, 0.1, 1,$ and 10. The results show that at low Reynolds numbers ($Re = 0.01, 0.1$), optimal non-Newtonian and Newtonian design topologies differ significantly, resulting in dual and merged pipes, respectively. At larger Reynolds numbers ($Re = 1$ and 10), both the non-Newtonian and Newtonian optimization results lead to similar designs (merged pipes), as would be expected due to the decreasing importance of non-Newtonian effects at higher Reynolds numbers. This decreasing shear-rate dependent effect on the viscosity is shown explicitly for the four non-Newtonian
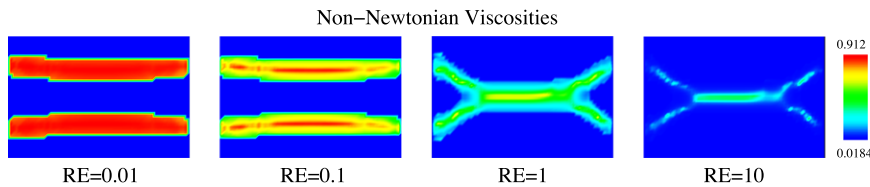
Non−Newtonian Viscosities

| RE=0.01 | RE=0.1 | RE=1 | RE=10 |

Fig. 8. Illustration of the decreasing non-Newtonian effects on flow viscosity with increasing Reynolds number for the non-Newtonian optimal designs at $Re = 0.01, 0.1, 1, 10$.

Table 1
Non-Newtonian design cross-comparison for coefficient of pressure: Optimal designs at each Reynolds number are indicated in bold.

Reynolds number	Dual-channel	Merged-channel
0.01	**9678.8e5**	12976e5
0.1	**908.16e5**	1033.5e5
1	56.738e5	**49.974e5**
10	2.3582e5	**1.8629e5**

Table 2
Newtonian design cross-comparison for coefficient of pressure: Optimal designs at each Reynolds number are indicated in bold.

Reynolds number	Dual-channel	Merged-channel
0.01	1072.8e5	**759.62e5**
0.1	108.64e5	**76.014e5**
1	10.868e5	**7.6531e5**
10	1.2160e5	**0.84110e5**

designs in Fig. 8. While the global optimality of the obtained results cannot be guaranteed, a cross-comparison for non-Newtonian (Table 1) and Newtonian (Table 2) flows between dual and merged pipes at the four Reynolds numbers shows that the obtained results are indeed optimal in comparison.

The physical response of the non-Newtonian design at $Re = 0.01$ for both non-Newtonian and Newtonian flow is visualized in Fig. 9. It can be seen that the difference of streamlines is minimal between the two flow models. However, the differences in pressure and velocity are more significant. The non-Newtonian velocities are larger near the boundaries to increase the boundary velocity gradient, decreasing the viscosity. Given the porous nature of the boundary and the relatively coarse mesh for the design, the no-slip boundary conditions are only approximately enforced. The pressure plots show that the non-Newtonian pressure drop is approximately 10 times larger than the Newtonian counter-part due to the increased non-Newtonian viscosities. In addition, it should be noted that irregularities exist in the non-Newtonian pressure plots close to the boundaries, a similar phenomenon to the velocity artifacts previously shown in Fig. 4, and an effect that will be further investigated by the authors.

Finally, a mesh refinement comparison between optimal non-Newtonian designs at $Re = 0.01$ for three meshes (30×20, 60×40, and 120×80) is shown in Fig. 10. The mesh refinement study suggests that the obtained optimal designs are mesh-independent, with the main difference being the reduced porous boundary effects for finer meshes.

5. Conclusions

In this paper, we have introduced a topology optimization approach for non-Newtonian flows based on the lattice Boltzmann method and the Carreau–Yasuda model for non-Newtonian fluids. We have presented a scaling of the non-Newtonian effects in order to overcome flow instabilities caused by the coupling of the LBM porosity and non-Newtonian flow models. While resulting in steady flows, the scaling of the non-Newtonian effects introduces artifacts (e.g. velocity banding) in the computed flow fields and requires further study. The obtained optimal results for a dual-pipe flow topology optimization problem illustrate the significant differences between optimal designs for Newtonian and non-Newtonian flows at small Reynolds numbers. Further studies are needed to explore the application of the introduced non-Newtonian topology optimization framework to 2D and 3D biomedical problems (e.g. maximizing wall shear-stress to reduce blood clotting) and to fluids with different non-Newtonian properties.
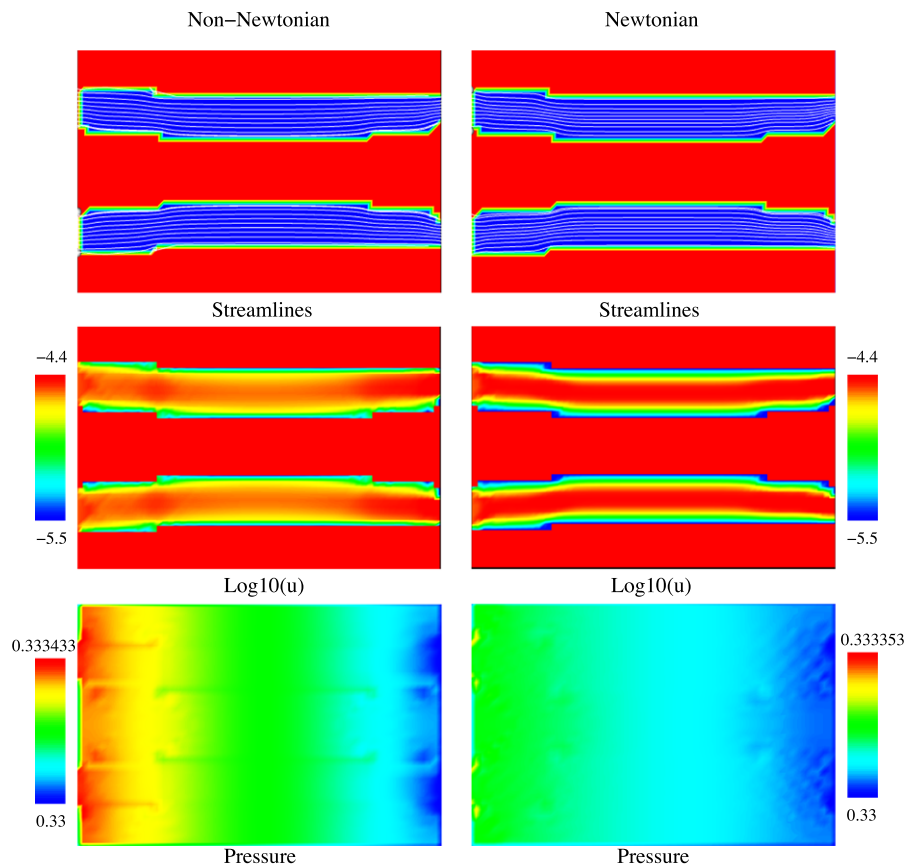
Acknowledgments

Fig. 9. Physical response (streamlines, velocity, and pressure) of non-Newtonian design at $Re = 0.01$ for both non-Newtonian and Newtonian flow. Both the streamline and 'log10' velocity plots are overlayed onto a plot of the design.
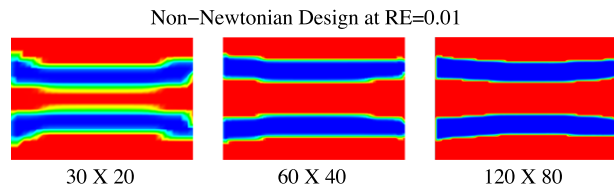

Fig. 10. Comparison between the non-Newtonian optimal design at $Re = 0.01$ on three meshes (30×20, 60×40, and 120×80) showing a mesh independent optimal design.

References

[1] F. Abraham, M. Behr, M. Heinkenschloss, Shape optimization in steady blood flow: A numerical study of non-Newtonian effects, Computer Methods in Biomechanics and Miomedical Engineering 8 (2) (2005) 127–137.

[2] F.J.H. Gijsen, F.N. van de Vosse, J.D. Janssen, The influence of the non-Newtonian properties of blood on the flow in large arteries: Steady flow in a carotid bifurcation model, Journal of Biomechanics 32 (1999) 601–608.

[3] A. Leuprecht, K. Perkold, Computer simulation of non-Newtonian effects on blood flow in large arteries, Computer Methods in Biomechanics and Biomedical Engineering 4 (2001) 149–163.

[4] M. Lukacova-Medvidova, A. Zauskova, Numerical modelling of shear-thinning non-Newtonian flows in compliant vessels, International Journal for Numerical Methods in Fluids 56 (2008) 1409–1415.

[5] J. Boyd, J.M. Buick, Comparison of Newtonian and non-Newtonian flows in a two-dimensional carotid artery model using the lattice Boltzmann method, Physics in Medicine and Biology 52 (2007) 6215–6228.

[6] A. Quarteroni, G. Rozza, Optimal control and sape optimization of aorto-coronaric bypass anastomoses, Mathematical Models and Methods in Applied Sciences 13 (2003) 1801–1823.

[7] J.F. Antaki, O. Ghattas, G.W. Burgreen, B. He, Computational flow optimization of rotary blood pump components, Artificial Organs 19 (1995) 608–615.

[8] T. Borrvall, J. Petersson, Topology optimization of fluids in Stokes flow, International Journal for Numerical Methods in Fluids 41 (1) (2003) 77–107.

[9] A. Gersborg-Hansen, O. Sigmund, R. Haber, Topology optimization of channel flow problems, Structural and Multidisciplinary Optimization 30 (3) (2005) 181–192.

[10] N. Wiker, Topology optimization in fluid flow problems, Ph.D. thesis, Department of Mechanical Engineering, Linköping University, 2006.

[11] M. Thellner, Multi-parameter topology optimization in continuum mechanics, Ph.D. thesis, Division of Mechanics, Department of Mechanical Engineering, Linköpings University, 2005.

[12] J.K. Guest, J.H. Prévost, Topology optimization of creeping fluid flows using a Darcy–Stokes finite element, International Journal for Numerical Methods in Engineering 66 (2006) 461–484.

[13] A. Evgrafov, On the limits of porous materials in the topology optimization of Stokes flows, Applied Mathematics and Optimization 52 (3) (2005) 263–277.

[14] A. Evgrafov, Topology optimization of slightly compressible fluids, ZAMM: Zeitschrift für Angewandte Mathematik und Mechanik 86 (1) (2005) 46–62.

[15] G. Pingen, A. Evgrafov, K. Maute, Topology optimization of flow domains using the lattice Boltzmann method, Structural and Multidisciplinary Optimization 34 (2007) 507–524.

[16] G. Pingen, A. Evgrafov, K. Maute, A parallel Schur complement solver for the solution of the adjoint steady state lattice Boltzmann equations: Application to design optimization, International Journal of Computational Fluid Dynamics 22 (2008) 457–464.

[17] G. Pingen, A. Evgrafov, K. Maute, Parameter sensitivity analysis for the hydrodynamic lattice Boltzmann method with applications to design optimization, Computers and Fluids 38 (2009) 910–923.

[18] J. Boyd, J.M. Buick, S. Green, Analysis of the Casson and Carreau–Yasuda non-Newtonian blood models in steady and oscillatory flows using the lattice Boltzmann method, Physics of Fluids 19 (2007) 093103:1–093193:14.

[19] D. Yu, R. Mei, L.-S. Luo, W. Shyy, Viscous flow computations with the method of lattice Boltzmann equation, Progress in Aerospace Sciences 39 (2003) 329–367.

[20] S. Succi, The Lattice Boltzmann Equation: For Fluid Dynamics and Beyond, in: Numerical Mathematics and Scientific Computation, Oxford University Press, 2001.

[21] S. Chen, G.D. Doolen, Lattice Boltzmann method for fluid flows, Annual Review of Fluid Mechanics 30 (1998) 329–364.

[22] D.A. Wolf-Gladrow, Lattice-Gas Cellular Automata and Lattice Boltzmann Models: An Introduction, in: Lecture Notes in Mathematics, Springer, 2000.

[23] P. Angot, C.-H. Bruneau, P. Fabrie, A penalization method to take into account obstacles in viscous flows, Numerical Mathematics 81 (1999) 497–520.

[24] H.C. Brinkmann, A calculation of the viscous force exerted by a flowing fluid on a dense swarm of particles, Applied Scientific Research Section A 1 (1947) 27.

[25] M.A.A. Spaid, F.R. Phelan, Lattice Boltzmann methods for modelling microscale flow in fibrous porous media, Physics of Fluids 9 (9) (1997) 2468–2474.

[26] H. Fang, Z. Wang, Z. Lin, M. Liu, Lattice Boltzmann method for simulating the viscous flow in large distensible blood vessels, Physical Review E 65 (2002) 051925:1–051925:11.

[27] S. Gabbanelli, G. Drazer, J. Koplik, Lattice Boltzmann method for non-Newtonian (power–law) fluids, Physical Review E 72 (2005) 046312:1–046312:7.

[28] D. Kehrwald, Lattice Boltzmann simulation of shear-thinning fluids, Journal of Statistical Physics 121 (1–2) (2005) 223–237.

[29] A.M. Artoli, Mesoscopic computational haemodynamics, Ph.D. thesis, University van Amsterdam, October 2003.

[30] P. Lallemand, L.-S. Luo, Theory of the lattice Boltzmann method: Dispersion, dissipation, isotropy, Galilean invariance, and stability, Physical Review E 61 (2000) 6546–6562.

[31] M. Reiner, The Deborah number, Physics Today 17 (1) (1964) 62.

[32] K. Svanberg, A globally convergent version of MMA without linesearch, in: G. Rozvany, N. Olhoff (Eds.), First World Congress of Structural and Multidisciplinary Optimization, Pergamon, 1995, pp. 9–16.